

Atomic mechanism and prediction of hydrogen embrittlement in iron

Jun Song¹ and W. A. Curtin²*

Hydrogen embrittlement in metals has posed a serious obstacle to designing strong and reliable structural materials for many decades, and predictive physical mechanisms still do not exist. Here, a new H embrittlement mechanism operating at the atomic scale in α -iron is demonstrated. Direct molecular dynamics simulations reveal a ductile-to-brittle transition caused by the suppression of dislocation emission at the crack tip due to aggregation of H, which then permits brittle-cleavage failure followed by slow crack growth. The atomistic embrittlement mechanism is then connected to material states and loading conditions through a kinetic model for H delivery to the crack-tip region. Parameter-free predictions of embrittlement thresholds in Fe-based steels over a range of H concentrations, mechanical loading rates and H diffusion rates are found to be in excellent agreement with experiments. This work provides a mechanistic, predictive framework for interpreting experiments, designing structural components and guiding the design of embrittlement-resistant materials.

The embrittling effects of H on the mechanical properties of structural metals have been well recognized for more than one century¹ and often lead to premature or catastrophic failure. Hydrogen embrittlement has thus been an important issue in industrial applications and attracted enormous research attention for decades^{2–4}, and is particularly severe in steels because of the high mobility of H in Fe. Many mechanisms have thus been proposed. H-enhanced decohesion^{5,6} (HEDE) postulates that H atoms attracted to the crack tip simply lower the fracture energy and thus encourage cleavage-like failure. However, this can occur only if the stress intensity for fracture is reduced below the value at which dislocation emission occurs, which is the competing deformation mode that leads to crack blunting and defeats cleavage-like fracture. Even at full saturation of interstitial H on the cleavage plane ahead of a crack in α -Fe, dislocation emission remains easier^{7–9}. Nonetheless, HEDE-like concepts have been used to qualitatively interpret experiments on pre-cracked Fe-based specimens^{6,8,10} but the analyses involved many assumptions; our modelling here generally supports one of the HEDE-like concepts proposed in ref. 10. H-enhanced local plasticity^{11–13} (HELP) is based on transmission electron microscopy observations of changes in dislocation pile-ups with and without H (refs 14,15) and of fracture surfaces showing high local plastic-like deformation in embrittled materials and slip bands at crack tips¹⁶. However, contradictory results exist^{17,18} and there is no direct connection between the proposed HELP-type mechanism and actual embrittlement. In general, physically based mechanisms leading to quantitative predictions of embrittlement do not yet exist.

Atomistic simulations have been used to test or to suggest nanoscale mechanisms for H embrittlement^{19–25}. The validity of simulations rests on the availability of accurate interatomic potentials, and potentials used in previous studies on the Fe–H system have not been fully validated. Molecular dynamics studies are also typically performed at very high loading rates (for example, ref. 19), which minimizes or eliminates important kinetic processes, such as H diffusion to the crack tip, and can lead to highly loaded configurations that the material would never attain under

normal experimental conditions. Putting such limitations aside, no simulations so far have made any quantifiable predictions of embrittlement nor any comparisons to experiment.

Here, we demonstrate a new embrittlement concept in which the accumulation of H around a crack tip, driven by the crack-tip stress fields, suppresses crack-tip dislocation emission and thus eliminates the ability of the material to blunt cracks. Fracture then occurs by the only remaining energy-relieving mechanism of cleavage, facilitated by the brittle nature of the H-rich material around the crack tip. We show operation of this new mechanism using extensive atomistic simulations of crack-tip behaviour in Fe in the presence of H, using a validated interatomic potential (see Supplementary Section S2) and including the kinetics of H diffusion and aggregation to the crack tip before, during and after the observed cleavage fracture. We connect this nanoscale mechanism to macroscopic embrittlement as a function of material properties and testing conditions using an analytic model for the H transport, and thus are able to identify the boundary between embrittlement and non-embrittlement as a function of H concentration, H diffusion, temperature and mechanical loading rate. Our parameter-free, mechanistic model is then applied to various H embrittlement experiments conducted across a range of ferritic steels^{26–30} using tensile/disc rupture tests on notched or unnotched samples. The excellent agreement between model predictions and experimental data demonstrates that our model provides fundamental and predictive insight into H embrittlement in Fe.

We examine the atomistic behaviour of nanoscale crack tips in α -Fe for two crack-tip geometries with orientations (crack plane normal) [crack front direction] of (111) [11 $\bar{2}$] (orientation I) and (111) [1 $\bar{1}$ 0] (orientation II), with periodicity along the crack front. Both orientations have a dislocation slip system, {11 $\bar{2}$ }(111) for orientation I and {1 $\bar{1}$ 0}(111) for orientation II, available for easy dislocation emission and thus represent the most ductile orientations for α -Fe. The crack is loaded by applying displacements on the outer boundary of the overall simulation cell according to the anisotropic elastic mode I stress intensity

¹Materials Engineering, McGill University, Montreal, Quebec H3A 2B2, Canada, ²Institute of Mechanical Engineering, EPFL, CH-1015 Lausanne, Switzerland. *e-mail: william.curtin@epfl.ch

field K_I (ref. 31). The system is initially deformed to a load $K_I = 0.8 \text{ MPa m}^{1/2}$ that provides a driving force for H segregation towards the crack tip but is small enough that no crack-tip phenomena (cleavage or dislocation emission) occur. H atoms are then randomly inserted into tetrahedral interstitial sites within a cylindrical region of radius 10 nm around the crack tip at a rate of 1 atom per picosecond. This process simulates the arrival of H atoms, through diffusion, from the far-field into the near-crack-tip region. After adding every 100 H atoms, the system is relaxed for 4 ns to allow H segregation and obtain a stable H configuration. After a desired total amount of H has been introduced, the crack is then loaded further by successive increments of 0.016, each followed by relaxation for 2 ns to allow redistribution of the H through diffusion. With a migration barrier of 0.04 eV, attempt frequency of $\sim 2.6 \times 10^{13} \text{ s}^{-1}$ (ref. 32) and at temperature $T = 300 \text{ K}$, each H in a perfect crystal would diffuse a distance $d \sim 20 \text{ nm}$ during each relaxation period; thus, all of the H atoms have ample time to move throughout the entire crack-tip region. Furthermore, various other sequences and procedures for introducing H and loading the crack give the same results. The fracture events at the crack tip (dislocation emission, brittle cleavage, other phenomena) are then investigated as a function of the applied load, the number of H atoms introduced and the extent of H aggregation around the crack tip. Note that this simulation strategy uses molecular dynamics to naturally generate a sequence of near-equilibrium H configurations around the crack tip that would occur at various times, far-field H concentrations and experimental loading rates, and the mechanical response of such configurations is then measured; the simulations thus bridge the timescale gap that often arises in attempting to connect molecular dynamics studies to experiments.

The results of our simulations are as follows. H atoms first segregate to the crack surfaces (Figs 1a and 2a), which is thermodynamically favourable but largely irrelevant to embrittlement. We thus consider the crack-tip behaviour as a function of the total amount N_H of bulk (that is, non-surface) H, per unit crack length, in the atomistic system. After the surfaces are saturated, H starts to aggregate in the vicinity of the loaded crack tip, driven by the energy of interaction between the volume misfit of the H interstitials in the Fe lattice and the high tensile pressure field near the mode-I crack. With increasing N_H , a H-rich region forms around the crack tip (Fig. 1). In orientation I, a wedge-shaped H-rich region, of atomic concentration between 0.6 and 0.8 per Fe atom, forms below the crack surface along the direction where either twinning or dislocation emission would occur in the absence of H. The aggregation and local fields ultimately induce a local body-centred cubic to face-centred cubic (bcc \rightarrow fcc) phase transformation in the H-rich region (Fig. 1b,c) that could occur through the reverse Bain mechanism³³. A limited amount of twinning is also observed very near the crack tip but cannot grow owing to the H-rich region. The crack-tip behaviour is greatly modified in the presence of H. Figure 3 shows the number N_H of bulk H atoms, per unit length L_z along the crack line, introduced into the simulation cell versus the stress intensity at which some crack-tip event occurs. There are three distinct regimes. In regime I ($0 \leq N_H/L_z < 35 \text{ nm}^{-1}$), the crack tip deforms by emitting a full edge dislocation of Burgers vector $[111]/2$, just as in pure Fe (Fig. 1a). No crack growth is observed in spite of high local H concentrations, so the HEDE mechanism^{5,6} does not operate. Increasing H increases the critical K_I for emission, so that HELP-like H-induced dislocation emission does not operate³⁴. In regime II ($35 \text{ nm}^{-1} \leq N_H/L_z < 122 \text{ nm}^{-1}$), the H-rich region blocks dislocation emission and instead, with increasing applied load, brittle cleavage occurs (Fig. 1b). In regime III ($N_H/L_z \geq 122 \text{ nm}^{-1}$), the H-rich region extends ahead of the crack tip and intersects the crack front and extensive brittle cleavage occurs, along with

emission of a single $[\bar{1}\bar{1}\bar{1}]/2$ dislocation (Fig. 1c). We expect that any H-rich region would block dislocation emission, so that the formation of a new phase, here fcc, is not crucial to the mechanism but does affect the load levels at which the transition to cleavage is observed. The observation of a crack-tip ductile-to-brittle transition induced by H aggregation at the crack tip is the first main result of this paper.

We have also examined the behaviour on further loading after the first crack-tip phenomenon occurs, while maintaining a fixed total number of H atoms. In regime I, loading beyond the critical K_I leads to emission of additional $[111]/2$ edge dislocations and blunting of the crack tip; that is, the ductile response of pure Fe. In regimes II–III, we observe slow crack growth where the crack remains sharp and within the H-rich region, which, through diffusion of the H atoms, moves with the crack tip (Fig. 1d). As the total H is fixed in the simulation, the size of the H-rich region shrinks and N_H decreases as H atoms segregate to the new crack surfaces until, at $N_H/L_z \sim 26 \text{ nm}^{-1}$, dislocation emission and crack-tip blunting resume, as found in regime I. The direct simulation of a slow-crack-growth embrittlement process, following the ductile-to-brittle transition, is the second main result of this paper.

The behaviour for orientation II is qualitatively similar to that for orientation I. Orientation II is on the ductile–brittle border even without H: at $T = 0 \text{ K}$, dislocation emission is observed whereas at $T = 300 \text{ K}$ cleavage is observed (see Supplementary Information). In regime I ($0 \leq N_H/L_z < 11 \text{ nm}^{-1}$), cleavage is thus observed at $T = 300 \text{ K}$ (Fig. 2a). In regime II ($11 \text{ nm}^{-1} \leq N_H/L_z < 260 \text{ nm}^{-1}$), H predominately aggregates directly below or above the fracture surface into a H-rich region with 0.6–0.8 H per Fe atom, which induces a local bcc to hexagonal close-packed (hcp) transformation (Fig. 2b). The critical deformation event changes from cleavage to emission of a full edge $[111]/2$ dislocation away from the HCP region (Fig. 2b). Evidently, the stresses induced by the H-rich region tilt the delicate balance in this orientation to favour emission over cleavage, but this H-enhanced emission has no connection to embrittlement. With further H loading, a second H-rich region with an embedded bcc \rightarrow hcp transformation forms on the other side of the crack tip. The critical deformation event remains emission but at increasing stress intensity. In regime III ($N_H/L_z \geq 260 \text{ nm}^{-1}$), the H-rich regions are large enough to suppress dislocation emission and enable cleavage along a deflected crack plane (Fig. 2c) so that the ductile-to-brittle transition is again observed. Under further loading, regime I shows continued cleavage, regime II shows emission of more dislocations and blunting of the crack tip and regime III shows slow crack growth (Fig. 2d), with the H atoms diffusing along with the crack tip until depletion of the H is sufficient to halt growth. This observation of the ductile–brittle transition fully supports the second main result of this paper.

To relate the atomistic simulations of H-induced embrittlement by H aggregation at the crack tip to macroscopic measurement of embrittlement, we now determine the rate of accumulation of H at the crack tip due to diffusion from further away. We consider temperature T , bulk equilibrium H concentration c_0 (related to an imposed H chemical potential) defined here on a per Fe atom basis, H diffusion coefficient D , and loading rate \dot{K}_I . H diffuses into the crack-tip region owing to the energetic driving force created by the chemical potential^{35,36}

$$\mu = \mu_0 + k_B T \ln \frac{c}{1-c} + p\Omega; \quad p(r, \theta) = \frac{2(1+\nu)}{3\sqrt{2\pi r}} \dot{K}_I t \cos \frac{\theta}{2}$$

where $p\Omega$ is the interaction between the crack-tip pressure field $p(r, \theta)$ and the partial volume Ω of an H interstitial in Fe, and c is the local atomic concentration of H at position (r, θ) . Noting that $c \ll 1$ away from the immediate crack-tip region, the average radial

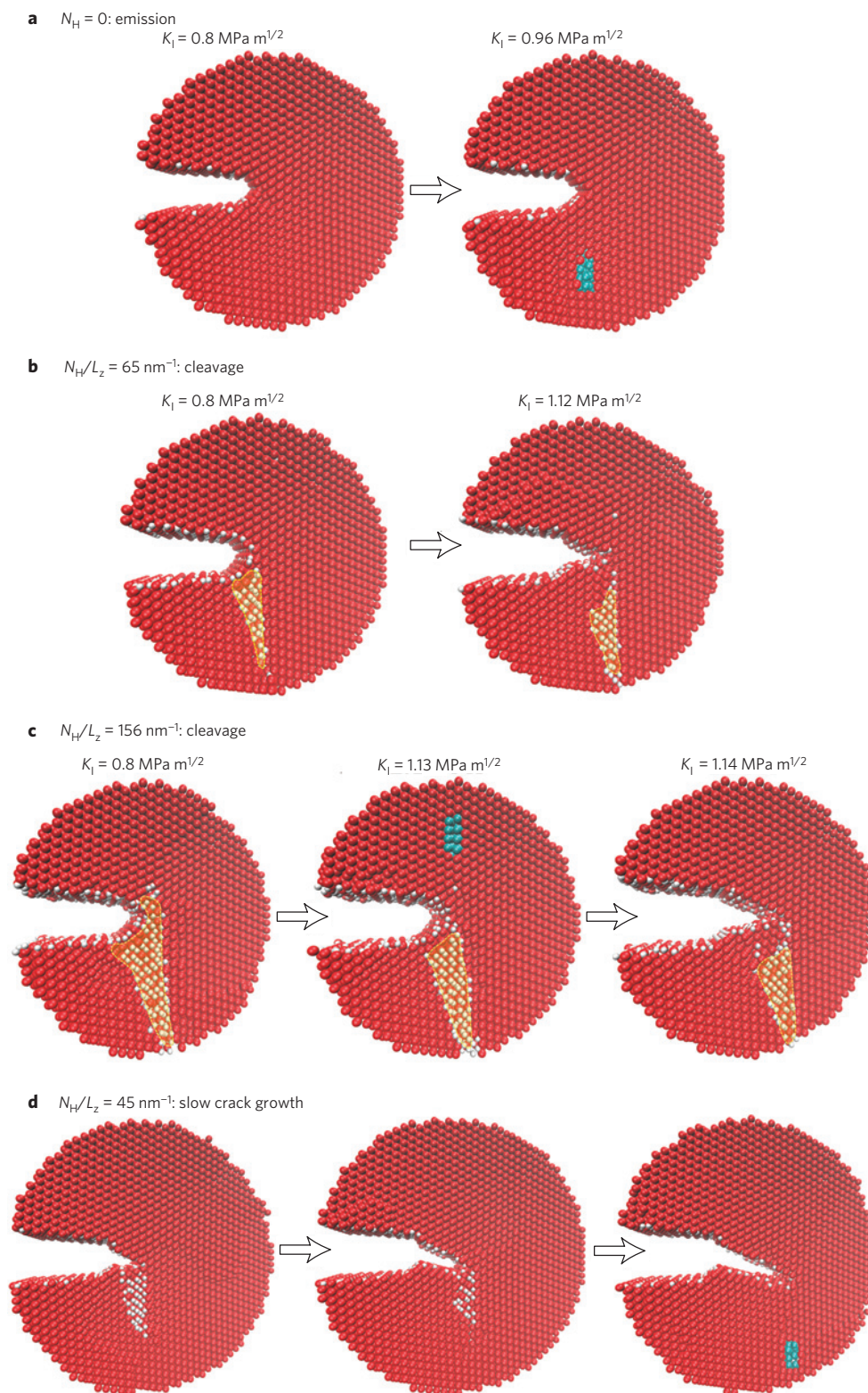


Figure 1 | Atomic configurations of the near-crack-tip region, shown as views along the crack line, for orientation I at various levels of H and applied load. H atoms are coloured white, and Fe atoms are coloured red, except for those in a dislocation core coloured cyan; shaded regions in **b,c** show areas of $\text{bcc} \rightarrow \text{fcc}$ phase transformation. **a**, For low amounts of H, H saturates the crack surfaces and the crack tip deforms through dislocation emission. **b**, For increased H, the H accumulates into a H-rich wedge-shaped region in the bulk near the crack tip, which evolves to induce a $\text{bcc} \rightarrow \text{fcc}$ phase transformation that blocks dislocation emission, and leads to brittle cleavage. **c**, Increased H leads to further growth of the H-rich region, which intersects the crack front and leads to emission of a single full dislocation of Burgers vector $[\bar{1}\bar{1}\bar{1}]/2$ followed immediately by brittle cleavage. **d**, Loading beyond the onset of cleavage leads to slow crack growth, where the H-rich region moves with the crack tip through diffusion; with a fixed amount of H, the H-rich region shrinks as H atoms are depleted by surface segregation until eventually it becomes so small that dislocation emission resumes.

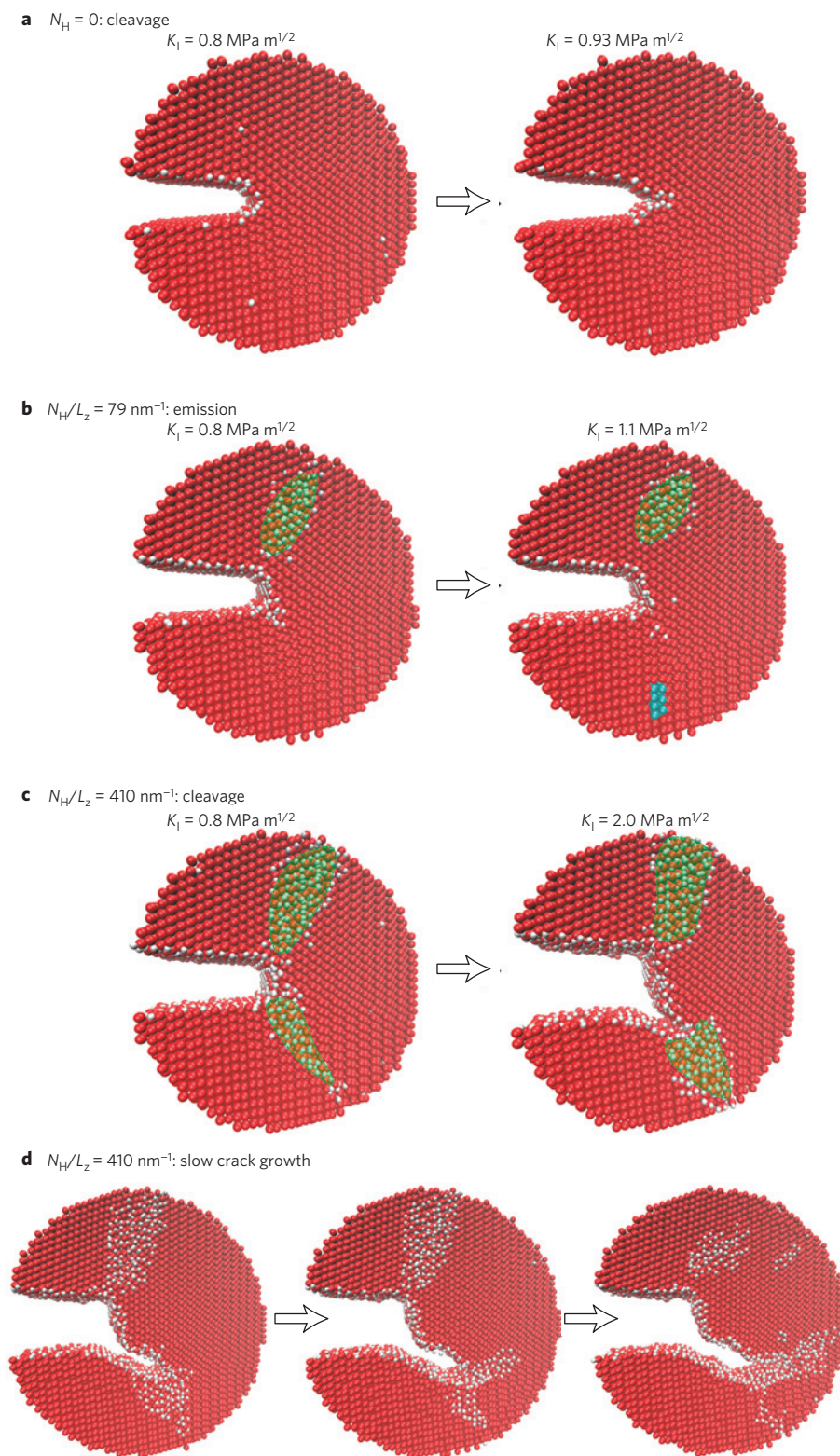


Figure 2 | Atomic configurations of the near-crack-tip region, shown as views along the crack line, for orientation II at various levels of H and load. The colour scheme is the same as that used in Fig. 1. **a**, For low amounts of H, H segregates to the crack surfaces and the crack tip deforms through brittle cleavage. **b**, For increased H, the H accumulates in the vicinity of the crack tip into a H-rich region predominately on one side of the crack, with a bcc \rightarrow hcp phase transformation within the H-rich region that inhibits dislocation emission from the same side but promotes emission from the other side. **c**, Further introduction of H atoms leads to the growth of the existing H-rich region and formation of a similar H-rich region on the opposite side of the crack, which suppresses dislocation emission and promotes brittle cleavage along a deflected crack plane. **d**, Further loading after cleavage leads to some rapid crack growth through the H-rich region followed by slow crack growth as the surrounding H atoms rearrange, including H atoms dissolving from the other H-rich region and aggregating around the new crack tip.

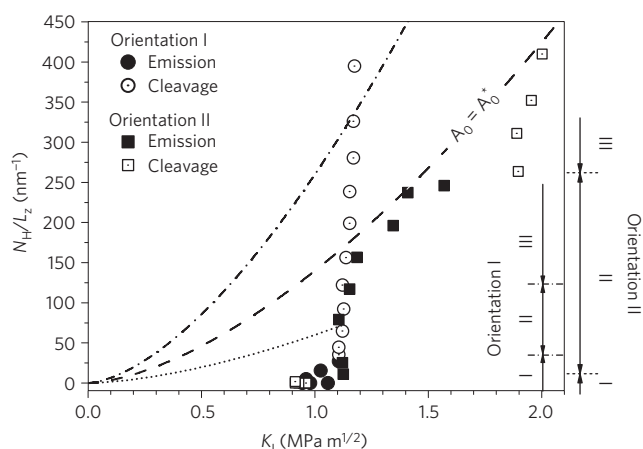


Figure 3 | The amount of H in the system normalized along the crack line direction, N_H/L_z , versus the stress intensity K_I at which either dislocation emission or brittle cleavage occurs, as found in simulations for orientations I and II. Filled symbols: dislocation emission; open symbols: brittle cleavage. The crack-tip behaviour for each orientation is partitioned into regimes I, II and III (see text). Also shown are the model predictions of N_H/L_z versus K_I for the critical value of the key parameter $A_0 = A_0^* = 1.4 \times 10^{11} \text{ MPa}^{-8/5} \text{ m}^{-9/5}$, which demarcates the boundary between conditions for which $A_0 > A_0^*$ (for example, dash-dotted line) ending in cleavage (brittle) and conditions for which $A_0 < A_0^*$ (for example, dotted line) ending in dislocation emission and crack blunting (ductile).

velocity of H atoms towards the crack tip is then

$$V_r = -\frac{D}{k_B T} (\nabla \mu)_r = \frac{(1+\nu) D \Omega \dot{K}_I t \cos(\theta/2)}{3\sqrt{2\pi} r^{3/2}}$$

As $V_r = -dr/dt$, after a time t all H within a radius $r = R$ can arrive at the crack tip $r \sim 0$, where

$$R = \left(\frac{5(1+\nu) D \Omega \dot{K}_I t^2 \cos(\theta/2)}{12\sqrt{2\pi} k_B T} \right)^{2/5} \quad (1)$$

The number N_H/L_z of H atoms per unit crack length near the crack tip at time t is then

$$N_H/L_z = \frac{2c_0}{a_0^3} \int_{-\pi}^{\pi} \frac{R^2}{2} d\theta = \beta \left(\frac{1}{2}, \frac{9}{10} \right) \frac{2c_0}{a_0^3} \left(\frac{5(1+\nu) D \Omega \dot{K}_I t^2}{12\sqrt{2\pi} k_B T} \right)^{4/5} \quad (2)$$

where $\beta(1/2, 9/10)$ is the beta function and a_0 is the lattice constant. The time needed for aggregation and redistribution of H near the crack tip is very small compared with the time needed for H to diffuse into the crack-tip region and so can be neglected. Substituting $K_I = \dot{K}_I t$ into equation (2), we obtain the near-crack-tip amount of H, N_H/L_z , as

$$N_H/L_z = A_0 K_I^{8/5}; A_0 = \beta \left(\frac{1}{2}, \frac{9}{10} \right) \frac{2c_0}{a_0^3} \left(\frac{5(1+\nu) D \Omega}{12\sqrt{2\pi} k_B T \dot{K}_I} \right)^{4/5} \quad (3)$$

In equation (3), A_0 is the single overall parameter that controls the kinetics of H aggregation at the crack due to any combination of loading, diffusion, concentration and temperature.

The simulations in Fig. 3 show that crack-tip phenomena occur along a locus of $(K_I, N_H/L_z)$ values. For any value of A_0 , equation (3) predicts the evolution of N_H/L_z as a function of the present value of K_I . There is a critical value, $A_0^* = 1.4 \times 10^{11} \text{ MPa}^{-8/5} \text{ m}^{-9/5}$, that divides the material response into ductile (dislocation emission) and brittle (cleavage) domains, as shown in Fig. 3. For $A_0 > A_0^*$, the

curve of N_H/L_z versus K_I intersects the simulations in the cleavage domain, and the material will be embrittled. $A_0 > A_0^*$ is the domain of high concentration, fast diffusion and/or slow loading rates, where there is sufficient transport of H to the crack to shut-off dislocation nucleation. For $A_0 < A_0^*$, the curve intersects in the emission domain (or mixed emission/cleavage domain), and the material will remain ductile. $A_0 < A_0^*$ is the domain of low concentration, slow diffusion and/or high loading rate, where there is insufficient transport of H into the crack-tip region to suppress dislocation emission in both of the most favourable orientations for emission. The prediction of H embrittlement in Fe for any material and loading conditions for which $A_0 > A_0^*$ is the third main result of this paper.

We now compare our quantitative parameter-free theory to literature data on embrittlement in a range of ferritic steels for which the required material and loading conditions are provided^{26–30}. For the experimental data, the material is considered to be embrittled if there is a clear transition in threshold stress intensity, toughness or the reduction of area, or the reduction of area is larger than 60%. For H in Fe, $\nu = 0.31$, $\Omega = 3.818 \text{ \AA}^3$ and $a_0 = 2.86 \text{ \AA}$. For the diffusion coefficient D , we use either the value measured in the experiment or the value listed in the steel handbook for steels of the same grade. For unnotched samples loaded in simple tension at strain rate $\dot{\epsilon}$, the microstructural grain size d is assumed as an effective flaw size in the material and the loading rate is calculated as $\dot{K}_I = E \dot{\epsilon} \sqrt{2\pi d}$, where E is Young's modulus. All values used here are shown in Table 1 and vary over a large range (factors of $\sim 3,000$ for $c_0 \sim 60$ for $D \sim 10$ for d , and ~ 300 for loading rate) across the scope of materials considered. Using the data in Table 1, we compute the value of A_0 and predict embrittlement in samples for which $A_0/A_0^* > 1$, as shown in Table 1. Our predictions agree very well with the experiments, with some experiments quite close to, and on the correct side of, the predicted brittle–ductile transition. Only one material, 10XX steel²⁹, is not predicted correctly, but just a small change to $A_0^* = 1.6 \times 10^{11} \text{ MPa}^{-8/5} \text{ m}^{-9/5}$ would lead to the prediction of embrittlement for the 60% cold work (CW) estimate for this sample while leaving all other predictions unchanged. Although accurate values for all of the necessary material parameters are difficult to obtain, the agreement shown in Table 1 contains no fitting parameters. The success of our model against a range of experiments is the fourth main result of this paper.

Embrittlement requires sustainment of the slow-crack-growth process after the initial cleavage event. Growth at rate \dot{a} requires supply of H atoms at the rate of $2\dot{a}/a_0^2$ per unit crack width. To grow the crack by length Δa requires diffusion of extra H from within a radius $R_{\Delta a} = (\Delta a a_0 / \pi c_0)^{1/2}$. Using our transport analysis above at the embrittlement stress intensity K_I , the time required for the H at this radius to reach the crack tip is

$$t(\Delta a) = \int_0^{R_{\Delta a}} dr / V_r = \frac{2}{5} \left(\frac{2 D \Omega (1+\nu) K_I}{\pi k_B T 3\sqrt{2\pi}} \right)^{-1} \left(\frac{a_0 \Delta a}{\pi c_0} \right)^{5/4}$$

where we have used the angular average of V_r in equation (1). $t(\Delta a)$ is also the total time of crack growth up to this point. The crack growth rate is then

$$\dot{a} = \frac{d\Delta a}{dt} = \frac{4 D \Omega (1+\nu) K_I}{\pi k_B T 3\sqrt{2\pi}} \left(\frac{\pi c_0}{a_0} \right)^{5/4} \Delta a^{-1/4} \quad (4)$$

The average crack growth rate decreases very slowly with increasing Δa , and can be estimated by the initial value ($\Delta a = a_0$). Using the values in Table 1, the maximum sustainable crack growth rates range from 10^{-8} to 10^{-4} m s^{-1} , with H being harvested from a region of only $R \sim 160 \text{ nm}$ around the crack tip at $c_0 = 1 \text{ appm}$. These growth rates are consistent with experimental rates of $\sim 10^{-8}$ – 10^{-4} m s^{-1} in single-crystal Fe–Si (refs 10,37), although these experiments show alternating cleavage and dislocation

Table 1 | Material parameters governing embrittlement in a range of experiments on H embrittlement in steels, the computed embrittlement parameter A_0 and the observed and predicted embrittlement ($A_0/A_0^* > 1$).

Material	c_0 (appm)	T (K)	D ($10^{-11} \text{ m}^2 \text{ s}^{-1}$)	d (μm)	Loading rate	A_0 ($\text{MPa}^{-8/5} \text{ m}^{-9/5}$)	A_0/A_0^*	Embrittlement	
								Observed	Predicted (Y/N)
X42 (ref. 27)	0.12	298	2.7 (ref. 45)	~ 30	$7.7 \times 10^{-7} - 7.7 \times 10^{-6} \text{ s}^{-1}$	$1.88 \times 10^{12} - 1.19 \times 10^{12}$	13.5–84.9	Y	Y
X42 (ref. 30)	0.06	298	2.7 (ref. 45)	~ 30	$4.6 \times 10^{-4} \text{ s}^{-1}$	3.55×10^{10}	0.2	N	N
X52 (ref. 29)	0.16	298	2.7 (ref. 45)	~ 10	$3 \times 10^{-4} \text{ s}^{-1}$	1.18×10^{11}	0.8	N	N
A516 Gr70 (ref. 29)	0.16	298	2.0 (ref. 46)	~ 20	$1.6 \times 10^{-4} \text{ s}^{-1}$	1.99×10^{11}	1.4	Y	Y
A516 Gr70 (ref. 29)	0.06	298	2.0 (ref. 46)	~ 20	$4.6 \times 10^{-4} \text{ s}^{-1}$	7.54×10^{10}	0.5	N	N
AERMET 100 (ref. 26)	5.6	296	0.2	11	$2.2 \times 10^{-4} \text{ MPa m}^{1/2} \text{ s}^{-1}$	2.40×10^{14}	1,713	Y	Y
AERMET 100 (ref. 26)	217	296	0.2	11	$0.7 \text{ MPa m}^{1/2} \text{ s}^{-1}$	1.47×10^{13}	105	Y	Y
AERMET 100 (ref. 26)	217	296	0.2	11	$1 \times 10^3 \text{ MPa m}^{1/2} \text{ s}^{-1}$	4.39×10^{10}	0.3	N	N
10XX (ref. 29)	0.51	298	12.2 (0% CW)	~ 100 (ref. 48)	$3.3 \times 10^{-5} \text{ s}^{-1}$	5.09×10^{12}	36.3	Y	Y
			2.0 (60% CW; ref. 47)			1.20×10^{12}	8.6	Y	Y
10XX (ref. 29)	0.16	298	12.2 (0% CW)	~ 100 (ref. 48)	$1 \times 10^{-4} \text{ s}^{-1}$	6.68×10^{11}	4.7	N	Y
			2.0 (60% CW; ref. 47)			1.56×10^{11}	1.1	N	Y

plasticity under nominal constant loading conditions. Our estimate is also a lower bound because diffusion near the crack can occur much faster, with a migration barrier of 0.04 eV due to the absence of traps, than over larger scales, where traps reduce the diffusivity and measured migration barriers are in the range $\Delta E_b^{\text{exp}} = 0.10\text{--}0.28$ eV (ref. 38). The slow-crack-growth rates we measure in the simulations are $\sim 1 \text{ nm}/100 \text{ ns} = 10^{-2} \text{ m}^{-1} \text{ s}^{-1}$, much faster than the estimate of equation (4) because the diffusion is that for pure Fe (no traps) and there is an initially plentiful supply of H around the crack tip. Last, we expect embrittlement to be preferential along grain boundaries. Although beyond the scope of this paper, grain boundaries will not influence the onset conditions for fracture, because suppression of dislocation emission requires accumulation of H in the crystalline regions around the crack tip on either side of the grain boundaries (ref. 36), but grain boundaries will influence slow crack growth through the larger supply and modified (that is, trapped or accelerated, depending on the grain boundaries) diffusion of H along the grain boundaries.

The mechanism proposed, demonstrated and validated here does not explain every experimental observation in the literature. However, although H can have many effects on the behaviour of a metal, some of these effects may not be directly related to, or the main driver of, the embrittlement. In particular, changes in dislocation plasticity due to H will certainly influence the plastic zone size and thus the macroscopic measured toughness, but do not directly connect to the cleavage-like, intergranular, brittle fracture typical of H embrittlement. We also have not explained experimental results on pre-existing cracks under nominally static loading^{6,8,10} but the mechanism identified and quantified here is consistent with the qualitative concepts advanced to explain those experiments, and we will pursue detailed application of our mechanism and associated theory to these conditions in the near future.

We have demonstrated an atomistic H embrittlement mechanism in Fe that provides both mechanistic insight into the embrittlement process and quantitative predictive capability. The mechanism, and its connection to material states and loading conditions through an analytic model, thus holds promise as a tool to identify operating regimes where embrittlement can be avoided in applications of existing materials and, ultimately, to guide the design of new embrittlement-resistant materials.

Methods

The molecular dynamics domains have dimensions $L_x \times L_y \times L_z$ of $485 \text{ \AA} \times 480 \text{ \AA} \times 24 \text{ \AA}$ and $480 \text{ \AA} \times 485 \text{ \AA} \times 28 \text{ \AA}$ for orientations I and II, respectively, where z lies along the crack front, y is normal to the crack plane and x is along the growth direction. The cracks are created by removing seven planes of atoms behind the crack tip. Molecular dynamics simulations are performed using the LAMMPS code³⁹. At $T = 300 \text{ K}$, an NVT ensemble with a Nosé–Hoover thermostat^{40,41} and velocity–Verlet algorithm⁴² with integration time steps of 0.4 and 2 fs for systems with and without H, respectively, are used. The interatomic interactions in the Fe–H system are described using a Finnis–Sinclair⁴³-type embedded-atom-method potential⁴⁴ modified in essential ways to avoid unphysical aggregation of H atoms in bulk Fe as described in the Supplementary Information.

Received 9 May 12; accepted 4 October 12; published online 11 November 2012

References

- Johnson, W. H. On some remarkable changes produced in iron and steels by the action of hydrogen acids. *Proc. R. Soc. Lond.* **23**, 168–175 (1875).
- Fukai, Y. *The Metal–Hydrogen System: Basic Bulk Properties* 2nd edn (Springer, 2005).
- Hardie, D., Charles, E. A. & Lopez, A. H. Hydrogen embrittlement of high strength pipeline steels. *Corros. Sci.* **48**, 4378–4385 (2006).
- Staehle, R. W. in *Stress Corrosion Cracking and Hydrogen Embrittlement of Iron Based Alloys* (eds Hochmann, J., McCright, R. D. & Slater, J. E.) (National Association of Corrosion Engineers, 1977).
- Troiano, A. R. The role of hydrogen and other interstitials in the mechanical behavior of metals. *Trans. ASM* **52**, 54–80 (1960).

6. Oriani, R. A. A mechanistic theory of hydrogen embrittlement of steels. *Ber. Bunsenges. Phys. Chem.* **76**, 848–857 (1972).
7. Jiang, D. E. & Carter, E. A. First principles assessment of ideal fracture energies of materials with mobile impurities: Implications for hydrogen embrittlement of metals. *Acta Mater.* **52**, 4801–4807 (2004).
8. Gerberich, W. W., Oriani, R. A., Lii, M. J., Chen, X. & Foecke, T. The necessity of both plasticity and brittleness in the fracture thresholds of iron. *Phil. Mag. A* **63**, 363–376 (1991).
9. Song, J., Soare, M. & Curtin, W. A. Testing continuum concepts for hydrogen embrittlement in metals using atomistics. *Model Simul. Mater. Sci.* **18**, 045003 (2010).
10. Chen, X. & Gerberich, W. W. The kinetics and micromechanics of hydrogen-assisted cracking in Fe₃ pct Si single-crystals. *Metall. Trans. A* **22**, 59–69 (1991).
11. Beacham, C. D. A new model for hydrogen-assisted cracking (hydrogen ‘embrittlement’). *Metall. Mater. Trans. B* **3**, 441–455 (1972).
12. Birnbaum, H. K. & Sofronis, P. Hydrogen-enhanced localized plasticity—a mechanism for hydrogen-related fracture. *Mater. Sci. Eng. A* **176**, 191–202 (1994).
13. Robertson, I. M. The effect of hydrogen on dislocation dynamics. *Eng. Fract. Mech.* **68**, 671–692 (2001).
14. Ferreira, P. J., Robertson, I. M. & Birnbaum, H. K. Hydrogen effects on the interaction between dislocations. *Acta Mater.* **46**, 1749–1757 (1998).
15. Sofronis, P. & Robertson, I. M. Transmission electron microscopy observations and micromechanical/continuum models for the effect of hydrogen on the mechanical behaviour of metals. *Phil. Mag. A* **82**, 3405–3413 (2002).
16. Abraham, D. P. & Altstetter, C. J. Hydrogen-enhanced localization of plasticity in an austenitic stainless-steel. *Metall. Mater. Trans. A* **26**, 2859–2871 (1995).
17. Abraham, D. P. & Altstetter, C. J. The effect of hydrogen on the yield and flow-stress of an austenitic stainless-steel. *Metall. Mater. Trans. A* **26**, 2849–2858 (1995).
18. Asano, S. & Otsuka, R. Lattice hardening due to dissolved hydrogen in iron and steel. *Scr. Metall. Mater.* **10**, 1015–1020 (1976).
19. Matsumoto, R., Taketomi, S., Matsumoto, S. & Miyazaki, N. Atomistic simulations of hydrogen embrittlement. *Int. J. Hydrogen Energy* **34**, 9576–9584 (2009).
20. Taketomi, S., Matsumoto, R. & Miyazaki, N. Atomistic study of the effect of hydrogen on dislocation emission from a mode II crack tip in alpha iron. *Int. J. Mech. Sci.* **52**, 334–338 (2010).
21. Hu, Z., Fukuyama, S., Yokogawa, K. & Okamoto, S. Hydrogen embrittlement of a single crystal of iron on a nanometre scale at a crack tip by molecular dynamics. *Model Simul. Mater. Sci.* **7**, 541–551 (1999).
22. Wen, M., Fukuyama, S. & Yokogawa, K. Atomistic simulations of effect of hydrogen on kink-pair energetics of screw dislocations in bcc iron. *Acta Mater.* **51**, 1767–1773 (2003).
23. Xu, X. J., Wen, M., Hu, Z., Fukuyama, S. & Yokogawa, K. Atomistic process on hydrogen embrittlement of a single crystal of nickel by the embedded atom method. *Comput. Mater. Sci.* **23**, 131–138 (2002).
24. Von Pezold, J., Lymperakis, L. & Neugebauer, J. Hydrogen-enhanced local plasticity at dilute bulk H concentrations: The role of H–H interactions and the formation of local hydrides. *Acta Mater.* **59**, 2969–2980 (2011); **59**, 5868 (2011).
25. Chandler, M. Q. *et al.* Hydrogen effects on nanovoid nucleation in face-centered cubic single-crystals. *Acta Mater.* **56**, 95–104 (2008).
26. Thomas, R. L. S., Scully, J. R. & Gangloff, R. P. Internal hydrogen embrittlement of ultrahigh-strength AERMET 100 steel. *Metall. Mater. Trans. A* **34**, 327–344 (2003).
27. Hoover, W., Iannucci, J., Robinson, S., Spingarn, J. & Stoltz, R. Hydrogen compatibility of structural materials for energy storage and transmission *Report No. SAND80-8202* (Sandia National Laboratories, 1980).
28. Cialone, H. & Holbrook, J. in *Hydrogen Embrittlement: Prevention and Control, ASTM STP 962* (ed. Raymond, L) 134–152 (American Society for Testing and Materials, 1988).
29. San Marchi, C. & Somerday, B. Technical reference on hydrogen compatibility of materials *Report No. SAND2008-1163* (Sandia National Laboratories, 2008).
30. Hoover, W., Robinson, S., Stoltz, R. & Spingarn, J. *Hydrogen Compatibility of Structural Materials for Energy Storage and Transmission Final Report* (Sandia National Laboratories, 1981).
31. Cherepanov, G. P. *Mechanics of Brittle Fracture* (McGraw-Hill, 1979).
32. Ramasubramaniam, A., Itakura, M., Ortiz, M. & Carter, E. A. Effect of atomic scale plasticity on hydrogen diffusion in iron: Quantum mechanically informed and on-the-fly kinetic Monte Carlo simulations. *J. Mater. Res.* **23**, 2757–2773 (2008).
33. Hale, L. M. *et al.* Molecular dynamics simulation of delamination of a stiff, body-centered cubic crystalline film from a compliant Si substrate. *J. Appl. Phys.* **106** (2009).
34. Lynch, S. P. Environmentally assisted cracking—overview of evidence for an adsorption-induced localized-slip process. *Acta Metall. Mater.* **36**, 2639–2661 (1988).
35. Friedel, J. *Dislocations* 1st English edn (Pergamon, 1964).
36. Song, J. & Curtin, W. A. A nanoscale mechanism of hydrogen embrittlement in metals. *Acta Mater.* **59**, 1557–1569 (2011).
37. Vehoff, H. & Rothe, W. Overview 30 gaseous-hydrogen embrittlement in FeSi-single and Ni-single crystals. *Acta Metall. Mater.* **31**, 1781–1793 (1983).
38. Alefeld, G. & Völkl, J. *Hydrogen in Metals* (Springer, 1978).
39. Plimpton, S. Fast parallel algorithms for short-range molecular-dynamics. *J. Comput. Phys.* **117**, 1–19 (1995).
40. Hoover, W. G. Canonical dynamics—equilibrium phase-space distributions. *Phys. Rev. A* **31**, 1695–1697 (1985).
41. Nose, S. A unified formulation of the constant temperature molecular-dynamics methods. *J. Chem. Phys.* **81**, 511–519 (1984).
42. Swope, W. C., Andersen, H. C., Berens, P. H. & Wilson, K. R. A computer-simulation method for the calculation of equilibrium-constants for the formation of physical clusters of molecules—application to small water clusters. *J. Chem. Phys.* **76**, 637–649 (1982).
43. Finnis, M. W. & Sinclair, J. E. A simple empirical n-body potential for transition-metals. *Phil. Mag. A* **50**, 45–55 (1984).
44. Daw, M. S. & Baskes, M. I. Embedded-atom method—derivation and application to impurities, surfaces, and other defects in metals. *Phys. Rev. B* **29**, 6443–6453 (1984).
45. Babu, S. S. *et al.* *Hydrogen Pipeline R&D, Project Review Meeting* (Oak Ridge, 2005).
46. Luppó, M. I. & Ovejero Garcia, J. The influence of microstructure on the trapping and diffusion of hydrogen in a low-carbon steel. *Corros. Sci.* **32**, 1125–1136 (1991).
47. Huang, H. & Shaw, W. J. D. Hydrogen embrittlement interactions in cold-worked steel. *Corrosion* **51**, 30–36 (1995).
48. Bethlehem Steel Corporation *Modern Steels and their Properties: Carbon and Alloy Steel Bars and Rods*. (Bethlehem Steel Corporation, 1978).

Acknowledgements

The authors acknowledge partial support of this work by the US Office of Naval Research (grant # N00014-05-1-0504), by the General Motors/Brown Collaborative Research Lab on Computational Materials and by the NSERC Discovery grant (grant # RGPIN 418469-2012).

Author contributions

The project was planned and supervised by W.A.C. The simulations were performed and the data were collected by J.S. The results were analysed and discussed by J.S. and W.A.C. The manuscript was prepared by J.S. and W.A.C.

Additional information

Supplementary information is available in the online version of the paper. Reprints and permissions information is available online at www.nature.com/reprints. Correspondence and requests for materials should be addressed to W.A.C.

Competing financial interests

The authors declare no competing financial interests.

Reproduced with permission of the copyright owner. Further reproduction prohibited without permission.